RESEARCH ARTICLE

Parity Metamaterials and Dynamic Acoustic Mimicry

Jinjie Shi[1†], Hongchen Chu[2†], Aurélien Merkel[3], Chenkai Liu[1], Johan Christensen[4*], Xiaozhou Liu[1*], and Yun Lai[1*]

[1]MOE Key Laboratory of Modern Acoustics, National Laboratory of Solid State Microstructures, School of Physics, Collaborative Innovation Center of Advanced Microstructures, and Jiangsu Physical Science Research Center, Nanjing University, Nanjing 210093, China. [2]School of Physics and Technology, Nanjing Normal University, Nanjing 210023, China. [3]Université de Lorraine, CNRS, Institut Jean Lamour, F-54000 Nancy, France. [4]IMDEA Materials Institute, Calle Eric Kandel, 2, Getafe, 28906 Madrid, Spain.

*Address correspondence to: johan.christensen@imdea.org (J.C.); xzliu@nju.edu.cn (X.L.); laiyun@nju.edu.cn (Y.L.)

†These authors contributed equally to this work.

While parity transformation represents a fundamental symmetry operation in physics, its implications remain underexplored in metamaterial science. Here, we introduce a framework leveraging parity transformation to construct parity-inverted counterparts of arbitrary 3-dimensional meta-atoms, enabling the creation of parity-engineered metamaterial slabs. We demonstrate that the synergy between reciprocity and parity transformation, distinct from mirror operation, guarantees undistorted wave transmission across exceptional bandwidths, independent of structural configuration or meta-atom design specifics. Furthermore, these metamaterials exhibit dynamic acoustic mimicry capability, enabling adaptive blending of reflected signatures into surrounding environments while preserving transmitted wavefront integrity. Validated through numerical simulations and experimental prototypes, this breakthrough offers transformative potential for acoustic camouflage applications, particularly for sonar systems. Our findings reveal fundamental implications of parity transformation in artificial materials, establishing parity engineering as a paradigm for designing ultrabroadband functional materials with unprecedented operational versatility.

Introduction

Parity transformation, the symmetry operation [1] involving a change of the sign in all spatial coordinates, i.e., $(x,y,z) \rightarrow (-x,-y,-z)$, has many profound impacts in physics. Applying parity transformation to an arbitrary object creates its unique counterpart as a rotation of its mirror image with reversed chirality, as exemplified by a hand and its image in the mirror in Fig. 1A and B. Recently, parity–time (PT) symmetry [2–5] has been exploited to reveal the existence of exceptional points [6–11], opening a promising field of non-Hermitian physics [12]. However, to date, there has been little discussion on the possibility of applying parity transformation alone in acoustic metamaterials [13–20] and metasurfaces [21,22], which have markedly broadened the boundaries of acoustic materials [23–42] and enabled novel functions such as acoustic cloaks and illusions [23,24,29,42] over the past decades.

Sonar domes are widely used in air and underwater environments to house and protect sonars [43,44]. To ensure accurate signal acquisition, they are typically made of effectively homogeneous materials that support broadband undistorted transmission. However, this uniformity also retains the reflection signature of the protected sonars, making it impossible to acoustically blend into surrounding environments. On the other hand, conventional digital coding metasurfaces [45–52] can alter the reflection signature, but they typically block or disrupt transmission signals, thereby disabling the functionality of the sonar. Overall, it is highly desirable to achieve dynamic acoustic camouflages [42] in reflection while keeping the sonar function intact in an ultrabroad spectrum. This requires the combination of effective homogeneity and inhomogeneity in a single material, which has been seldomly discussed.

In this work, we apply parity transformation to design a class of acoustic metamaterials denoted parity metamaterials. Parity transformation relates an arbitrary 3-dimensional (3D) meta-atom with its unique parity-inverted counterpart. They constitute a pair of building blocks (Fig. 1C) for a special metamaterial slab called parity metamaterial (Fig. 1E), which can keep transmission wavefront undistorted in an extremely broad spectrum, while dynamically tuning the wavefront in reflection to mimic those from a periodic terrain, a rugged terrain, and a flat terrain, etc. These metamaterials thus enable dynamic acoustic mimicry (Text S1 and Fig. S1) to blend into the acoustic environment. At the same time, ultrabroadband undistorted transmission is guaranteed irrespective of the dynamical mimicry, which is extremely important for sonar detection. Therefore, this metamaterial offers
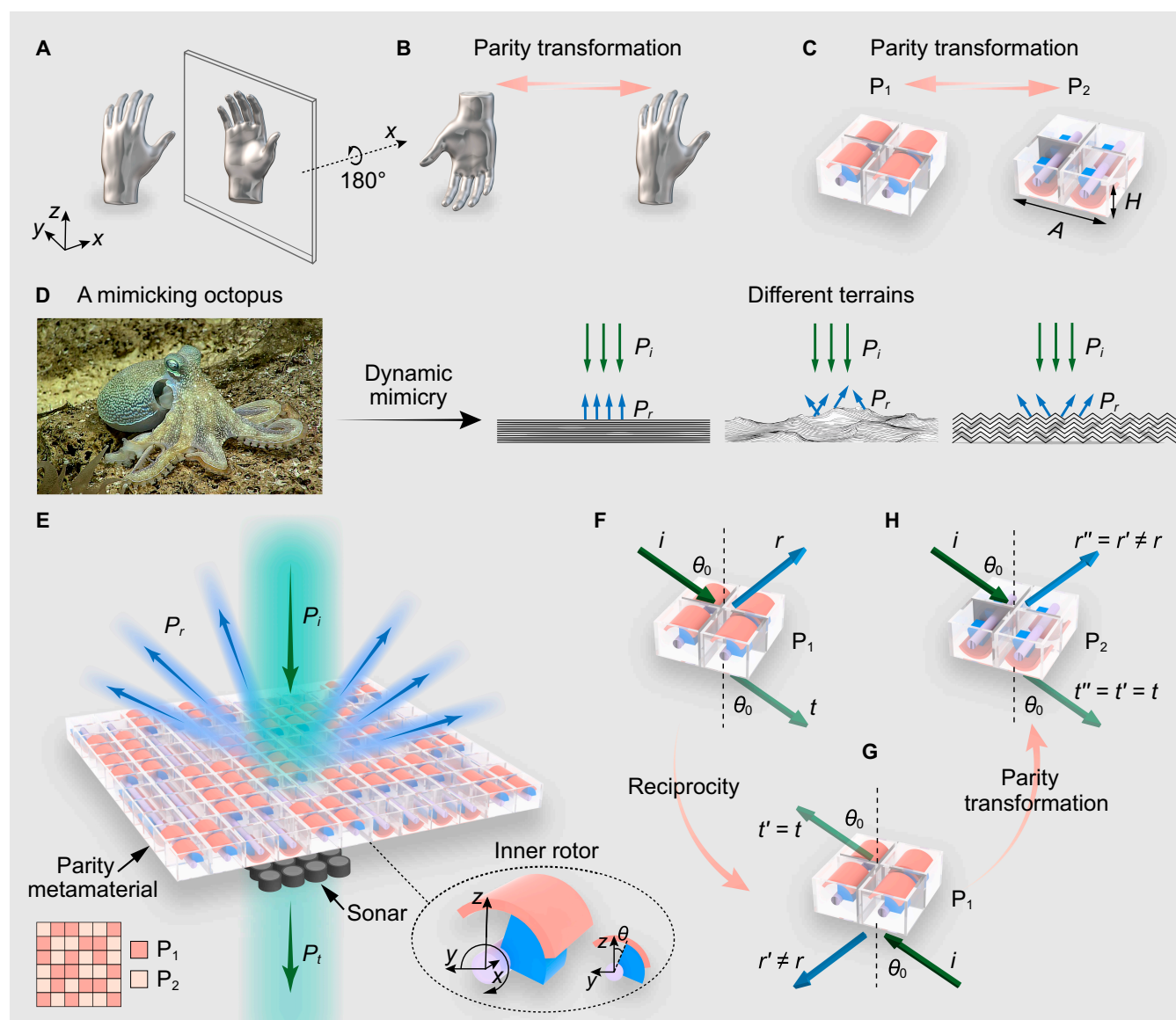
Fig. 1. A parity metamaterial composed of a meta-atom and its parity-inverted counterpart. (A and B) The hand, its mirror image, and its parity-inverted counterpart. The mirror image and the parity-inverted counterpart are related by a 180° rotation along the *x* axis. (C) The 3D meta-atom and its parity-inverted counterpart design related by parity transformation. (D) The concept of acoustic mimicry to imitate different terrains, including a flat terrain, a rugged terrain, and a periodic terrain, like an octopus. (E) The illustration of a parity metamaterial based on a random distribution of P_1 and P_2. Bottom right inset provides a magnified picture of the inner rotor. (F to H) Reciprocity and parity transformation rigorously prove that the meta-atom and its parity-inverted counterpart have the same transmission but different reflection coefficients.

a way to realize dynamic acoustic camouflage for advanced sonar systems, just like octopuses that can adapt their color and form to blend into their surroundings while still perceiving the environment (Fig. 1D). Our theory unveils the principle of parity engineering in metamaterials and metasurfaces, promising a profound impact in multiple disciplines.

Results

Theory and design of parity metamaterials

We consider an arbitrary 3D meta-atom and its parity-inverted counterpart, as denoted by P_1 and P_2, respectively. To accord with the working wavelength, the basic units of the metamaterial are composed of an array of 2×2 meta-atoms P_1 or P_2, as depicted in Fig. 1C. The adjacent basic units are separated by hard boundaries to minimize the coupling between them. The

length and thickness of the array are specified as $A = 60$ mm and $H = 24$ mm, respectively. To achieve dynamic tunability of the parity metamaterials, we designed the meta-atom and its parity-inverted counterpart to be rotatable. The magnified view of the inner rotor is displayed in the bottom-right inset of Fig. 1E. The curved plate can be rotated to tune the reflection phase, and the connection to the shaft is set to be asymmetric to remove all symmetry in the metastructure. The detailed parameters of the meta-atom can be found in Text S2 and Fig. S2. Figure 1E depicts the schematic diagram of the parity metamaterial slab composed of a selected arrangement of the meta-atom and its parity-inverted counterpart, which can tune the reflection while keeping transmission unaffected, if the system is reciprocal.

The underlying physical principle is described as follows. We first consider the scattering properties of this pair of

metastructures (P_1 and P_2), assuming that the transmission and reflection coefficients of P_1 in Fig. 1F are denoted as t and r, respectively. When the system is reciprocal, the reciprocity theorem [53–55] asserts that the exchange of the incidence and transmission channels does not change the transmission coefficient, i.e., $t' = t$, as shown in Fig. 1G. On the contrary, the reflection coefficient can differ markedly after the interchange, i.e., $r' \neq r$. Subsequently, we apply a parity operation to the system, as shown in Fig. 1H. P_1 is transformed into its counterpart, i.e., P_2, which has the same transmission coefficient as P_1, i.e., $t'' = t' = t$. This equivalence is regardless of the details of the metastructures, as well as the frequency and the incident angle. In reflection, contrarily, we have $r'' = r' \neq r$; thus, there is a phase difference between r' and r over a wide spectrum, which can modulate the reflection from this metamaterial. Moreover, the phenomena here can also be explained by a theory based on the transfer matrix method in stratified media (Text S3 and Fig. S3).

Ultrabroadband and wide-angle undistorted transmission

In the following, we present the transmission and reflection properties of P_1 and P_2. Figure 2A and B illustrates, respectively, the calculated transmittance and transmission phase, as well as the reflectance and reflection phase of P_1 and P_2, as functions of the frequency. The direction of the incident wave is along the z direction. Here, acoustic dissipation is neglected for simplicity,

but this principle also applies to general dissipated systems. From Fig. 2A, it is seen that the transmittance and transmission phase of P_1 and P_2 are identical over an ultrabroad spectrum ranging from 0.1 to 7 kHz (Text S4 and Fig. S4). The reflectance is also the same, but there is a substantial difference in the reflection phase, as depicted in Fig. 2B. In particular, the phase difference, $\Delta\varphi_r$, reaches the maximum value of 180° at a frequency of 5.68 kHz (denoted by a gray vertical line). By rotating P_1 and P_2 simultaneously, the phase difference in reflection can be conveniently tuned. Figure 2C illustrates the reflection phase difference between P_1 and P_2, i.e., $\Delta\varphi_r$, as a function of the rotation angle of the rotor and frequency, which covers the whole range of 360° around 5.68 kHz. The black dashed line represents the condition of $\Delta\varphi_r = 180°$. We emphasize that rotation does not change the condition of equal transmittance and $\Delta\varphi_t = 0°$ over the whole spectrum from 0.1 to 7 kHz (Text S5 and Fig. S5). This condition guarantees that the transmitted acoustic wavefront is the same as that of the incidence in an ultrabroad spectrum, independent of the arrangement of P_1 and P_2.

To demonstrate this unique feature, we consider a parity metamaterial composed of randomly distributed P_1 and P_2 illuminated by an incident plane wave of different frequencies and incident angles. The arrangement of P_1 and P_2 is shown in the bottom-left inset of Fig. 1E. By using finite-element software COMSOL Multiphysics, the 3D far-field radiation power patterns in transmission are calculated under normal incidence at 2, 4, and 6 kHz, as shown in Fig. 2D. The direction of transmission (P_t) is the same
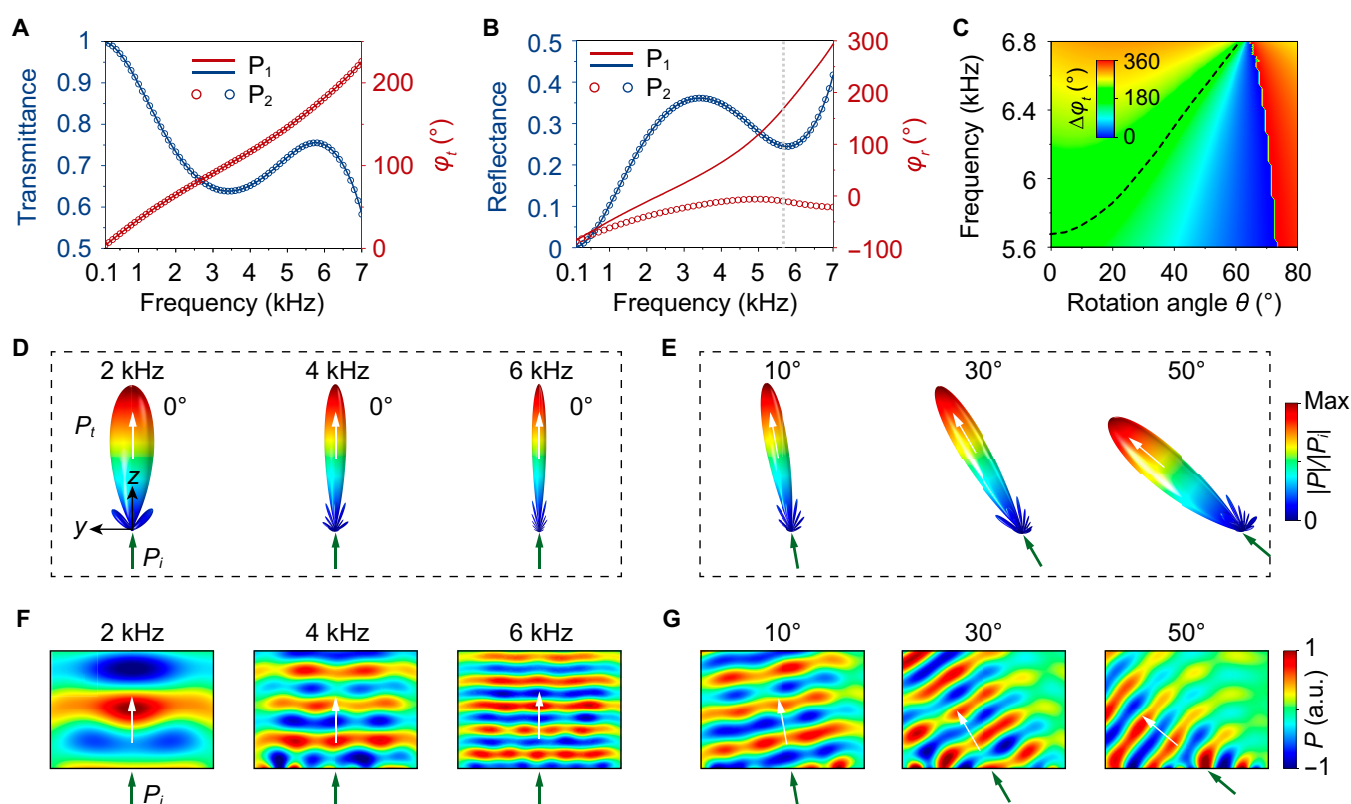

Fig. 2. Transmission and reflection properties of P_1 and P_2. (A) Transmittance and transmission phase spectra of P_1 and P_2. (B) Reflectance and reflection phase spectra of P_1 and P_2. (C) Reflection phase difference between P_1 and P_2 as a function of the rotation angle and frequency. (D) Simulated 3D far-field radiation power patterns in transmission under normal incidence at 2, 4, and 6 kHz. (E) Simulated 3D far-field radiation power patterns in transmission under incident angles of 10°, 30°, and 50° at 4 kHz. Each subpanel in (D) and (E) is normalized. (F to G) Simulated near-field distributions of the transmitted acoustic field in the yz plane. Here, the colors indicate the normalized pressure of the acoustic field. a.u., arbitrary units.

as that of the incidence (P_i) for all frequencies. In Fig. 2E, we plot the 3D far-field radiation power patterns in transmission for incident angles of 10°, 30°, and 50° at 4 kHz. It is observed that the direction of transmission (P_t) aligns consistently with the direction of incidence (P_i) for all angles. These effects are further verified by the calculated near-field distributions, as shown in Fig. 2F and G, respectively. In other words, such a disordered metamaterial functions like an ordered metamaterial in transmission, ensuring its feasibility in important applications such as acoustic detection and sonar technology [43,44,56].

Parity transformation versus mirror operation

To elucidate the essential role of parity transformation, we compare it with the mirror operation, i.e., upside-down flip, namely, $(x, y, z) \rightarrow (x, y, -z)$. When the metastructure exhibits a C_4^v symmetry in the xy plane, there is no difference between $(x, y, z) \rightarrow (-x, -y, -z)$ and $(x, y, z) \rightarrow (x, y, -z)$ [57,58]. However, the difference becomes huge when the metastructure

has no symmetry, which is the case here. Figure 3A depicts the schematic diagrams of P_1, P_2, and the structure generated by mirror operation, M_z, respectively. It is seen that M_z is different from P_2. In Fig. 3B and C, we plot the transmittance and transmission phase spectra of P_1, P_2, and M_z under the illumination of an incident angle of 30°, respectively, as shown by the green arrow in Fig. 3A. P_1 and P_2 have the same transmittance and transmission phase, as strictly protected by reciprocity and parity transformation. However, M_z and P_1 exhibit distinctly different transmission phase around 6.9 kHz. A comprehensive discussion is available in Text S6 and Fig. S6. The wide-angle transmission behaviors of P_1, P_2, and M_z are shown in Text S7 and Fig. S7.

Such a fundamental difference between parity transformation and mirror operation is further experimentally verified. We construct 2 metamaterials with the sequences $P_1P_2P_1P_2P_1P_2$ (case I) and $P_1M_zP_1M_zP_1M_z$ (case II), as illustrated in Fig. 3D and H, respectively. The simulated 3D far-field radiation power patterns in transmission for cases I and II under an incident
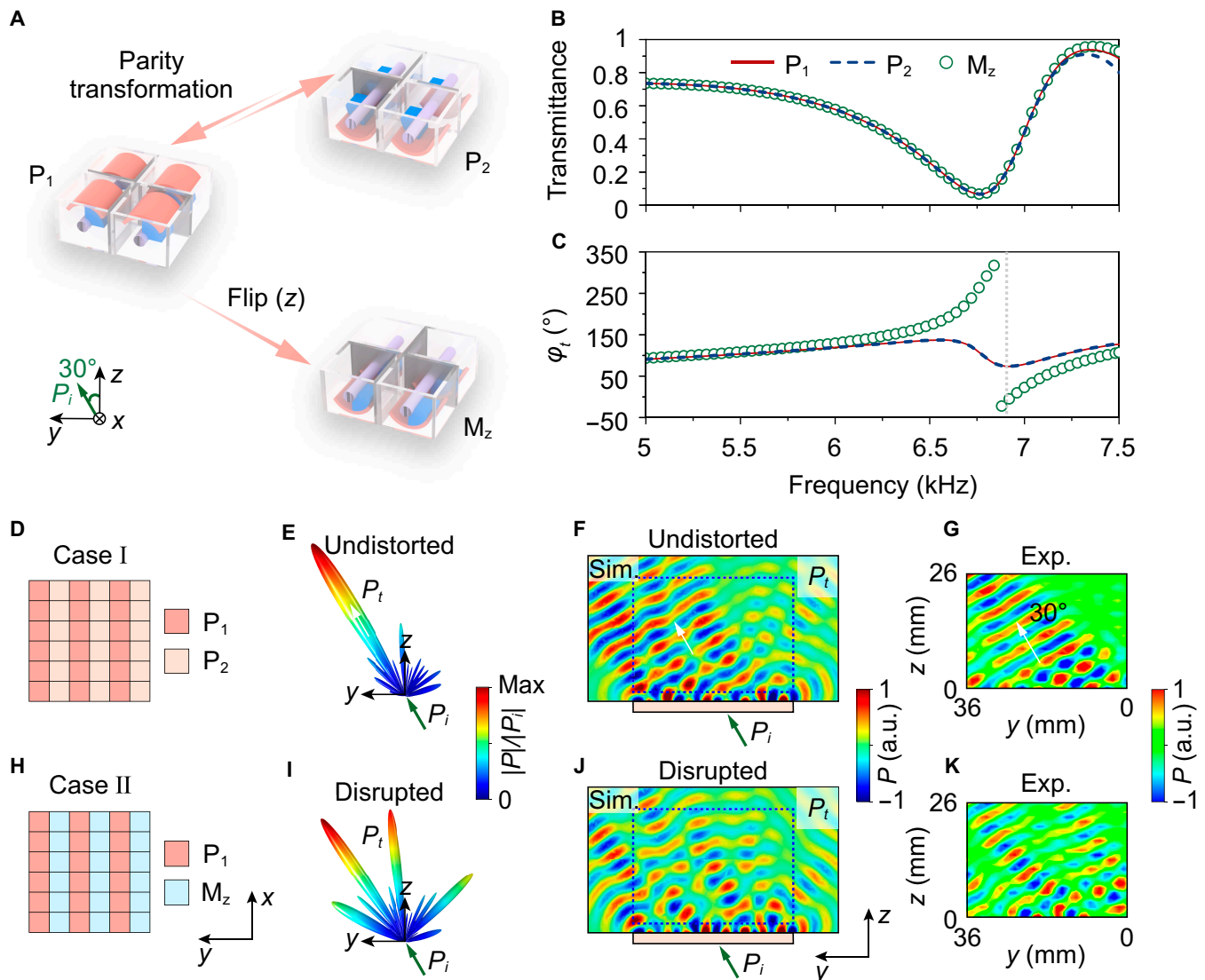
Fig. 3. Comparison between parity transformation and mirror operation. (A) Schematic diagrams of P_1, P_2, and M_z. M_z is the mirror image of P_1 along the z direction. (B and C) Transmittance and transmission phase spectra of P_1, P_2, and M_z under the illumination of an incident angle of 30°. (D and H) Metamaterial design for cases I and II, respectively. (E and I) Simulated 3D far-field radiation power patterns in transmission for cases I and II, respectively. (F, J, G, and K) Simulated (F and J) and measured (G and K) near-field distributions of the transmitted field for case I (F and G) and case II (J and K) in the yz plane.

angle of 30° at 6.9 kHz are shown in Fig. 3E and I, respectively. The transmitted wave (P_t) is undistorted in Fig. 3E but disrupted in Fig. 3I. Such a distinct difference originates in the transmission phase difference between P_1 (P_2) and M_z, which reaches 87° at 6.9 kHz (denoted by a gray vertical dotted line in Fig. 3C). This huge difference is also observed in the calculated and measured near-field distributions for cases I and II, as shown in Fig. 3F, G, J, and K, respectively. The measured regions are marked by the blue dotted boxes in the yz plane, as shown in Fig. 3F and J. The experimental and numerical results approximately agree with each other, both confirming that it is the parity transformation instead of the mirror operation that can preserve the transmission wavefront.

Dynamic acoustic mimicry

In the following, we numerically and experimentally demonstrate the realization of dynamic acoustic mimicry. By rotating the rotors of the designed parity metamaterial, it is possible to alter the reflection to emulate that from a periodic terrain, a rugged terrain, and a flat terrain, while keeping the transmission wavefront undistorted (Text S8 and Fig. S8). The insets of Fig. 4A portray the magnified views of the inner rotors of P_1 and P_2, wherein the rotors of both P_1 and P_2 are simultaneously rotated by the same angle, such that P_1 and P_2 can always be transformed into each other via parity transformation. Consequently, P_1 and P_2 always have identical transmittance (Fig. S9) and transmission phase (Fig. 4A), regardless of the rotation angle. On the other
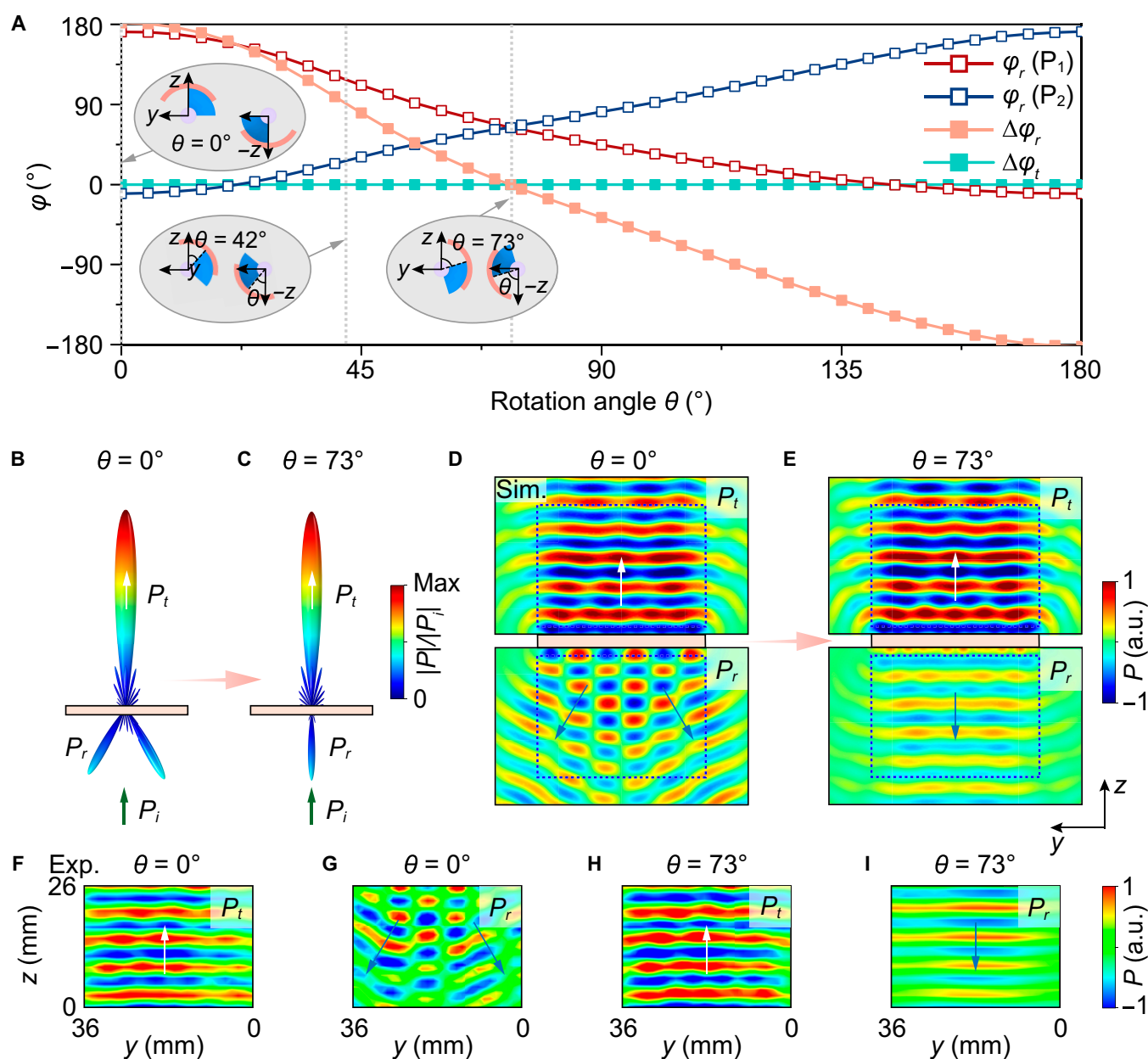

Fig. 4. Dynamic acoustic mimicry using a parity metamaterial. (A) Reflection phase spectra of P_1 and P_2 and their difference in reflection and transmission as functions of the rotation angle θ at 5.68 kHz. Insets show the magnified views of the inner rotors of P_1 and P_2. (B and C) Simulated 3D far-field radiation power patterns under normal incidence at 5.68 kHz for $\theta = 0°$ and $\theta = 73°$, respectively. (D and E) Simulated corresponding near-field distributions in the yz plane. (F to I) Measured acoustic field distributions of transmitted (F and H) and reflected (G and I) waves under normal incidence at 5.68 kHz when $\theta = 0°$ (F and G) and $\theta = 73°$ (H and I).

hand, the reflection phase difference between P_1 and P_2 varies markedly with the rotation angle. Figure 4A depicts the calculated reflection phase of P_1 and P_2, as well as their difference as functions of the rotation angle θ under normal incidence at a working frequency of 5.68 kHz. The reflection phase difference $\Delta\varphi_r$ varies from $-180°$ to $180°$, while the transmission phase difference $\Delta\varphi_t$ remains $0°$. This indicates that the rotation angle θ offers a freedom to dynamically tune the reflection without changing the transmission wavefront.

Here, we demonstrate the switching of reflection from 2-beam reflection to specular reflection, while maintaining undistorted transmission all the time. The parity metamaterial is the same as that shown in Fig. 3D. Figure 4B and C shows the simulated 3D far-field radiation power patterns under normal incidence at 5.68 kHz for $\theta = 0°$ and $\theta = 73°$ (denoted by gray vertical dotted lines in Fig. 4A), respectively. The direction of transmission (P_t) is the same as that of the incidence (P_i) for both cases. On the other hand, the reflection changes from the case of splitting into 2 beams (for $\theta = 0°$) to the case of specular reflection ($\theta = 73°$). This is because $\Delta\varphi_r$ changes from $180°$ to $0°$ when θ changes from $0°$ to $73°$. The switching phenomenon is further verified by simulated and measured near-field distributions, which are shown in Fig. 4D to I, respectively. The scanned areas correspond to the blue dotted boxes in Fig. 4D and E. The measured results coincide excellently with the numerical results, confirming that the transmitted wave (P_t) maintains a plane wavefront for the 2 cases. For reflection, the angle of reflection is $\theta_r = 30.2°$ $\{\theta_r = \sin^{-1}[\lambda/(2A)]\}$ (Text S9) at a rotation angle of $\theta = 0°$, as shown by the green arrows in Fig. 4D. The quantitative analysis of the transmission and reflection behaviors is shown in Text S10 and Fig. S11. In addition, the case for $\theta = 42°$ is shown in Text S8 and Fig. S10, displaying the simultaneous existence of 3-beam reflection and undistorted transmission. Therefore, dynamic acoustic mimicry can be realized using the rotation angle θ as an extra degree of freedom in the metastructure design.

We also demonstrated the cases of diffuse reflection and reflection holography (Texts S11 and S12 and Figs. S12 and S13). The results again confirm the conclusion: The acoustic reflection signatures can be freely altered to mimic the sophisticated acoustic environment, while keeping the transmitted wavefront unchanged in an ultrabroad spectrum, which is crucial for sonar. This functionality cannot be achieved by conventional digital coding metasurfaces [45–52] (Text S13 and Fig. S14).

Temporal acoustic camouflage

The integration of parity metamaterials with sonar systems offers the potential for temporal camouflage. This effect is vividly demonstrated by comparing the reflection signals of a Gaussian pulse incident on a sonar, both without and with a parity metamaterial. The pulse is a time-domain Gaussian signal with a duration of 1 s and a center frequency of 10 kHz. In accordance with the working wavelength, the basic units of the parity metamaterial are composed of only one meta-atom P_1 or its parity-inverted counterpart P_2, as shown in Fig. 5A. In our simulations, the sonar is modeled as an impedance boundary with an impedance of $38Z_0$, where Z_0 is the impedance of air. Under this condition, the simulated sonar provides approximately 90% reflection.

The parity metamaterial is closely attached to the sonar (just like the necessary sonar domes in practical sonar systems). In

this case, the reflections from the metamaterial and the sonar itself both influence the overall reflection. By meticulously adjusting the rotation angle θ of the rotors in the parity metamaterial, as well as the distance d between the metamaterial and the sonar, it is possible to achieve destructive interference between the reflections from the sonar and those from the parity metamaterial. This results in a substantial reduction of the overall signal. The mechanism behind the acoustic camouflage is illustrated in Fig. 5B. The total reflection R can be expressed as

$$R = r_1 + \sum_{n=1}^{\infty} t_1^2 r_1'^{\,n-1} r_2^n e^{-2in\varphi_d} = r_1 + t_1^2 r_2 e^{-2i\varphi_d}\left(1 - r_1' r_2 e^{-2i\varphi_d}\right)^{-1}$$
(1)

where r_1 and r_1' denote the reflection coefficients on the front and back interfaces of the parity metamaterial, r_2 is the reflection coefficient of the sonar, t_1 is the transmission coefficient of the parity metamaterial, and φ_d indicates the phase change through the air layer. By setting $R = 0$, the overall specular signal can be eliminated. Under this condition, we only need to consider the 0th-order transmission and reflection coefficients of the parity metamaterial and sonar. The phase shift can be expressed as $\varphi_d = kd$, where k is the wave number. For example, when the rotation angle of the rotors is $\theta = 75°$, the distance between the metamaterial and the sonar is calculated as $d = 5.9$ mm. The details are shown in Text S14 and Fig. S15.

Figure 5C shows the snapshots of the incident and reflected Gaussian pulse without the parity metamaterial. As expected, a strong specular reflection is observed when the pulse directly impinges on the sonar. In contrast, when the parity metamaterial covers the sonar, the specular reflection is substantially reduced, and the scatterings in other directions emerge, as shown in Fig. 5D. To quantify the temporal camouflage effect, we simulated the reflected signals received at a probe located at a certain distance from the sonar. The results, shown in Fig. 5E, demonstrate a marked reduction in the reflected signal intensity when the parity metamaterial is present. Specifically, the reflected signal strength is reduced to below 7% of its original value, and this value is expected to decrease further at greater distances. This effect makes the sonar system more difficult to be detected. Simultaneously, the parity metamaterial preserves the undistorted ultrabroadband transmission, ensuring the effectiveness of sonar detection.

Conclusion

We would like to emphasize that the concept of parity metamaterials is fundamentally different from PT-symmetric metamaterials. PT-symmetric metamaterials [2–5] are non-Hermitian systems with global PT symmetry, while the parity metamaterials do not require any global symmetry at all. On the other hand, PT-symmetric systems require delicately balanced loss and gain, while the functionalities of parity metamaterials are inherently robust to loss (Text S15 and Fig. S16) because both the reciprocity principle and parity transformation are uninfluenced by loss.

Parity metamaterials are fundamentally different from previously reported metamaterials studied in topological acoustics [59–63]. In topological systems, the wave behavior is governed by the bulk band structure, which arises from the periodic arrangement of a single type of unit cell with carefully designed internal symmetry and intercell coupling. These systems often exhibit edge-localized states, valley vortex fields, or other nontrivial band
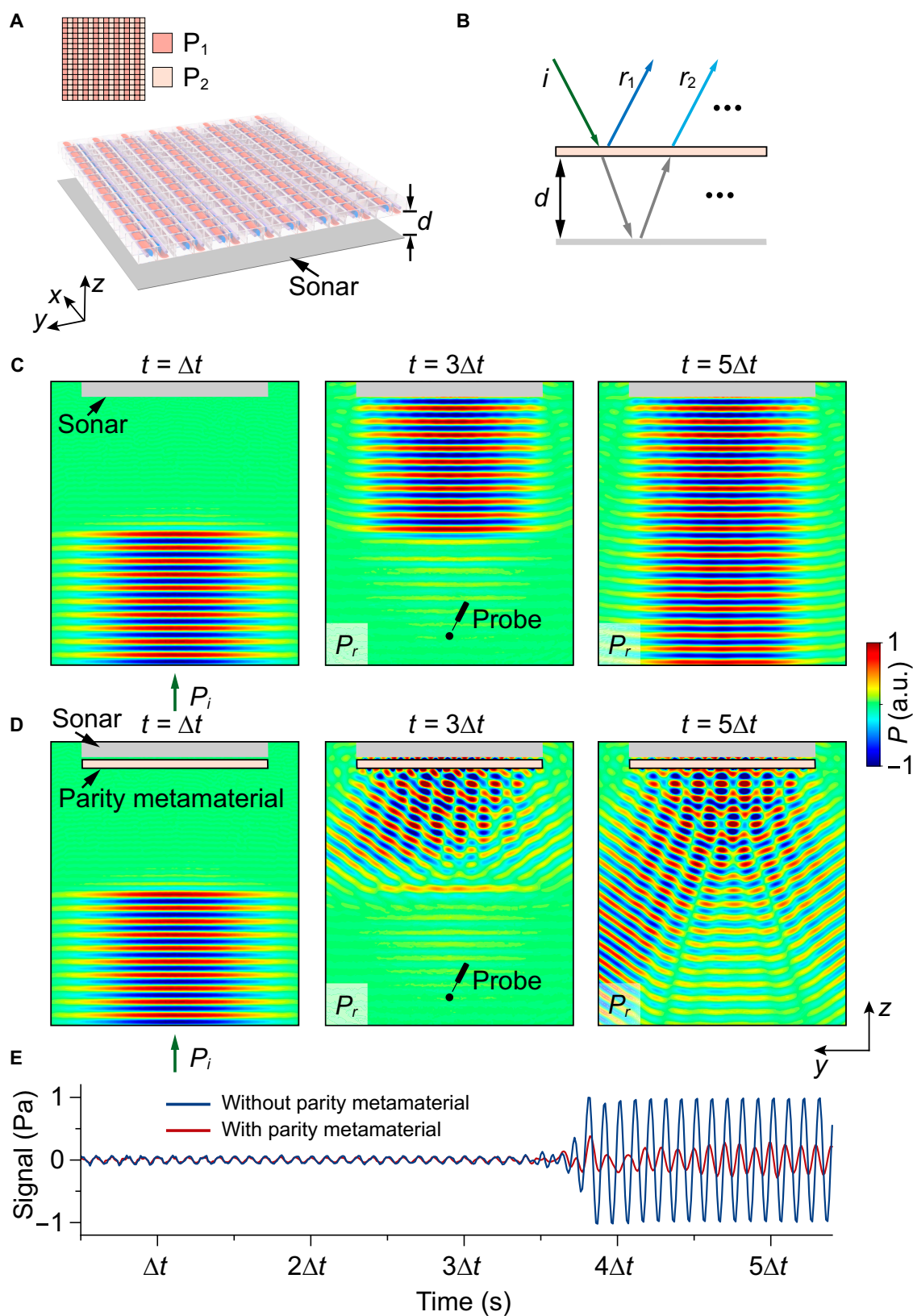
Fig. 5. Temporal acoustic camouflage via a sonar integrated with a parity metamaterial. (A) Schematic diagram of a sonar integrated with a parity metamaterial. Inset shows the design of the parity metamaterial. (B) The mechanism of the acoustic camouflage. (C and D) Snapshots of a Gaussian pulse incident on a sonar without (C) and with (D) a parity metamaterial, where $\Delta t = 1$ ms. The left panels of (C) and (D) show the incident pulse, while the middle and right panels display the reflected signals. (E) Simulated reflection signals received at the probe, both without and with a parity metamaterial.

topology effects. In contrast, parity metamaterials proposed here are constructed using a pair of meta-atoms, i.e., a meta-atom and its unique parity-inverted counterpart. Our design is not constrained by lattice periodicity and enables aperiodic arrangements, through which the reflection signature can be tailored. This mechanism unlocks a new class of wavefront control, wherein broadband undistorted transmission is guaranteed irrespective of tunable reflection shaping, enabling applications such as camouflaged sonar domes.

On the other hand, asymmetry has been recently adopted to achieve exceptional points for unidirectional absorption [64]. Here, asymmetry is applied in the design of meta-atoms for dynamic acoustic mimicry. The approach of parity metamaterials generally applies to meta-atoms of any symmetry. Compared with symmetric meta-atoms, asymmetric meta-atoms can provide many more degrees of freedom for tuning the reflection, thereby enabling dynamic acoustic mimicry.

We should note that parity metamaterials reveal the fundamental difference between parity transformation $(x, y, z) \rightarrow (-x, -y, -z)$ and mirror operation $(x, y, z) \rightarrow (x, y, -z)$, which was applied in previous optical metasurface designs [57,58]. This fundamental difference is manifested by the important advantage that parity metamaterials can be constructed from arbitrary building blocks, including ones with chirality and no symmetry at all, which is a huge advance in contrast to the previous optical designs. This difference also releases a large amount of new freedom that enables the dynamical acoustic mimicry, which can flexibly simulate the acoustic signatures of a periodic terrain, a rugged terrain, and a flat terrain, etc. Furthermore, the acoustic camouflage performance is also demonstrated in temporal domains.

In summary, we introduce the fundamental symmetry operation, parity transformation, to design a new class of metamaterials denoted as parity metamaterials. These metamaterials are constituted by an arbitrary 3D meta-atom and its unique parity-inverted counterpart. The combination of parity transformation and reciprocity allows for dynamic acoustic mimicry in reflection without distorting the transmitted wavefront across a wide spectrum. This approach is universal and applies to all types of structures and materials, as long as they are reciprocal. The constituent meta-atoms do not necessitate any specific symmetry and work robustly with loss. Although the demonstration here is conducted using airborne sound, it can also be extended to underwater scenarios (Text S16 and Fig. S17). It is also effective when the thickness of the metamaterial is much larger (Text S17 and Fig. S18). Our findings uncover the profound role of parity transformation in ultrabroadband wave manipulation, establishing parity engineering as a transformative paradigm for artificial material design, with implications spanning acoustic camouflage, adaptive metasurfaces, and next-generation communication systems.

Methods

Numerical simulations

The full-wave simulations are performed using the commercial finite element software COMSOL Multiphysics. In the calculations, the parameters of air are set as $\rho_0 = 1.21 \ \mathrm{kg/m^3}$ and $c_0 = 343 \ \mathrm{m/s}$. The impedance of air is $Z_0 = \rho_0 c_0 = 415.03 \ \mathrm{Pa \cdot s/m^3}$. The structures are fabricated using photopolymer resin, with a mass density $\rho = 1,300 \ \mathrm{kg/m^3}$ and speed of sound $c = 716 \ \mathrm{m/s}$. Acoustic impedance is $Z = \rho c \approx 9.3 \times 10^5 \mathrm{Pa \cdot s/m}$. Given that the acoustic impedance of air is approximately 415 Pa·s/m, this results in an impedance contrast exceeding 2,243×, which justifies the treatment of the resin as acoustically rigid. The background pressure field is used in Figs. 2 to 4. The periodic boundary condition is set in the x and y directions, and perfectly matched layers are adopted in the z direction to reduce the reflection. In Fig. 5, a Gaussian wave is utilized.

Experimental measurements

All samples are fabricated with resin using stereolithography 3D printing techniques (0.2 mm in precision). All the rotors are printed separately to facilitate rotational operations during the experiment. The rotor angles are manually adjusted using a standard protractor (angle ruler). Before each measurement, we align the rotor by visually matching the angle between the curved plate and a reference line with the aid of a handheld protractor. While this method is simple, it allows us to control the rotor angle with an estimated accuracy of ±2° to 3°. The whole size of the sample is 360 mm × 360 mm × 360 mm.

The experimental configuration is depicted in Fig. S19. To generate a quasi-plane wave, a speaker array (Five HiVi B1S) equipped with a parabolic mirror is meticulously constructed. A microphone (GRAS 46BE) is affixed to a movable stage to systematically scan the distribution of the acoustic field with a step size of 10 mm. To mitigate the influence of waves propagating around the specimen, sound-absorbing foams are affixed in its vicinity. The 2 measured regions on the sides of reflection and transmission in the xz-plane are shown as 2 blue rectangular areas in Fig. S19A. Both regions are 36 mm × 26 mm in size and are positioned 2 cm away from the sample. The photo of the experimental setup is shown in Fig. S19B. The measured reflected field distribution is obtained by subtracting the incident field (measured without the sample) from the total field (measured with the sample). The experiment is carried out in an anechoic room to minimize reflection and noise.

Data Availability

The data that support the plots within this paper and other findings of this study are available from the corresponding author upon reasonable request.

Supplementary Materials

Texts S1 to S17
Figs. S1 to S19

References

1. Livio M. Why symmetry matters. *Nature*. 2012;490(7421): 472–473.
2. Regensburger A, Bersch C, Miri M-A, Onishchukov G, Christodoulides DN, Peschel U. Parity-time synthetic photonic lattices. *Nature*. 2012;488(7410):167–171.
3. Feng L, Wong ZJ, Ma R-M, Wang Y, Zhang X. Single-mode laser by parity-time symmetry breaking. *Science*. 2014;346(6212):972–975.
4. Feng L, El-Ganainy R, Ge L. Non-Hermitian photonics based on parity-time symmetry. *Nat Photonics*. 2017;11:752–762.
5. El-Ganainy R, Makris KG, Khajavikhan M, Musslimani ZH, Rotter S, Christodoulides DN. Non-Hermitian physics and PT symmetry. *Nat Phys*. 2018;14(1):11–19.
6. Ding K, Ma G, Xiao M, Zhang ZQ, Chan CT. Emergence, coalescence, and topological properties of multiple exceptional points and their experimental realization. *Phys Rev X*. 2016;6(2):021007.
7. Miri M-A, Alù A. Exceptional points in optics and photonics. *Science*. 2019;363(6422):eaar7709.
8. Özdemir ŞK, Rotter S, Nori F, Yang L. Parity-time symmetry and exceptional points in photonics. *Nat Mater*. 2019;18(8):783–798.
9. Tang W, Jiang X, Ding K, Xiao Y-x, Zhang ZQ, Chan CT, Ma G. Exceptional nexus with a hybrid topological invariant. *Science*. 2020;370(6520):1077–1080.
10. Song Q, Odeh M, Zúñiga-Pérez J, Kanté B, Genevet P. Plasmonic topological metasurface by encircling an exceptional point. *Science*. 2021;373:1133–1137.
11. Ding K, Fang C, Ma G. Non-Hermitian topology and exceptional-point geometries. *Nat Rev Phys*. 2022;4: 745–760.
12. Wang W, Wang X, Ma G. Non-Hermitian morphing of topological modes. *Nature*. 2022;608(7921):50.
13. Liu Z, Zhang X, Mao Y, Zhu Y, Yang Z, Chan CT, Sheng P. Locally resonant sonic materials. *Science*. 2000;289:1734–1736.
14. Fang N, Xi D, Xu J, Ambati M, Srituravanich W, Sun C, Zhang X. Ultrasonic metamaterials with negative modulus. *Nat Mater*. 2006;5(6):452–456.
15. Liang Z, Li J. Extreme acoustic metamaterial by coiling up space. *Phys Rev Lett*. 2012;108(11):114301.
16. Cummer SA, Christensen J, Alù A. Controlling sound with acoustic metamaterials. *Nat Rev Mater*. 2016;1(3):16001.
17. Ma G, Sheng P. Acoustic metamaterials: From local resonances to broad horizons. *Sci Adv*. 2016;2(2):Article e1501595.
18. Yang M, Sheng P. Sound absorption structures: From porous media to acoustic metamaterials. *Annu Rev Mater Res*. 2017;47(1):83–114.
19. Ge H, Yang M, Ma C, Ming-Hui L, Chen Y-F, Fang N, Sheng P. Breaking the barriers: Advances in acoustic functional materials. *Natl Sci Rev*. 2018;5(2):159–182.
20. Zhang X, Xiao M, Cheng Y, Lu MH, Christensen J. Topological sound. *Commun Phys*. 2018;1:97.
21. Yang Z, Mei J, Yang M, Chan NH, Sheng P. Membrane-type acoustic metamaterial with negative dynamic mass. *Phys Rev Lett*. 2008;101:204301.

22. Assouar B, Liang B, Wu Y, Li Y, Cheng J-C, Jing Y. Acoustic metasurfaces. *Nat Rev Mater*. 2018;3(12):460–472.
23. Popa B-I, Zigoneanu L, Cummer SA. Experimental acoustic ground cloak in air. *Phys Rev Lett*. 2011;106:253901.
24. Zhang S, Xia C, Fang N. Broadband acoustic cloak for ultrasound waves. *Phys Rev Lett*. 2011;106(25): Article 024301.
25. Zhu J, Christensen J, Jung J, Martín-Moreno L, Yin X, Fok L, Zhang X, Garcia-Vidal FJ. A holey-structured metamaterial for acoustic deep-subwavelength imaging. *Nat Phys*. 2011;7: 52–55.
26. Mei J, Ma G, Yang M, Yang Z, Wen W, Sheng P. Dark acoustic metamaterials as super absorbers for low-frequency sound. *Nat Commun*. 2012;3:756.
27. Ma G, Yang M, Xiao S, Yang Z, Sheng P. Acoustic metasurface with hybrid resonances. *Nat Mater*. 2014;13(9):873–878.
28. Quan L, Zhong X, Liu X, Gong X, Johnson PA. Effective impedance boundary optimization and its contribution to dipole radiation and radiation pattern control. *Nat Commun*. 2014;5:3188.
29. Zigoneanu L, Popa B-I, Cummer SA. Three-dimensional broadband omnidirectional acoustic ground cloak. *Nat Mater*. 2014;13(4):352–355.
30. Li Y, Shen C, Xie Y, Li J, Wang W, Cummer SA, Jing Y. Tunable asymmetric transmission via Lossy acoustic metasurfaces. *Phys Rev Lett*. 2017;119(3):035501.
31. Zhu Y, Fan X, Liang B, Cheng J, Jing Y. Ultrathin acoustic metasurface-based Schroeder diffuser. *Phys Rev X*. 2017;7(2):021034.
32. Ma G, Fan X, Sheng P, Fink M. Shaping reverberating sound fields with an actively tunable metasurface. *Proc Natl Acad Sci USA*. 2018;115(26):6638–6643.
33. Zhu Y, Hu J, Fan X, Yang J, Liang B, Zhu X, Cheng J. Fine manipulation of sound via lossy metamaterials with independent and arbitrary reflection amplitude and phase. *Nat Commun*. 2018;9(1):1632.
34. Xu C, Ma G, Chen Z-G, Luo J, Shi J, Lai Y, Ying W. Three-dimensional acoustic double-zero-index medium with a fourfold degenerate Dirac-like point. *Phys Rev Lett*. 2020;124(7):074501.
35. Hu B, Zhang Z, Zhang H, Zheng L, Xiong W, Yue Z, Wang X, Xu J, Cheng Y, Liu X, et al. Non-Hermitian topological whispering gallery. *Nature*. 2021;597(7878): 655–659.
36. Liu C, Shi J, Zhao W, Zhou X, Ma C, Peng R, Wang M, Hang ZH, Liu X, Christensen J, et al. Three-dimensional soundproof acoustic Metacage. *Phys Rev Lett*. 2021;127(8):Article 084301.
37. Cao R, Guo G, Yue W, Huang Y, Li X, Kai C, Li Y, Tu J, Zhang D, Xi P, et al. Phase-dislocation-mediated high-dimensional fractional acoustic-vortex communication. *Research*. 2023;6:0280.
38. Han C, Fan S, Li C, Chen L-Q, Yang T, Qiu C-W. Nonlocal acoustic moiré hyperbolic metasurfaces. *Adv Mater*. 2024;36(18):2311350.
39. Tian Y-Z, Wei Z-R, Wang Y-F, Laude V, Wang Y-S. Adjustable phase-amplitude-phase acoustic metasurface for the implementation of arbitrary impedance matrices. *Research*. 2024;7:0502.
40. Zhou HT, Li CY, Zhu JH, Hu C, Wang YF, Wang YS, Qiu CW. Dynamic acoustic beamshaping with coupling-immune moiré metasurfaces. *Adv Mater*. 2024;36(24):Article 2313004.

41. Zou H-Y, Ge Y, Zhao K-Q, Lu Y-J, Si Q-R, Yuan S-Q, Chen H, Sun H-X, Yang Y, Zhang B. Acoustic metagrating holograms. *Adv Mater*. 2024;36(28):Article 2401738.
42. Liu C, Ma C, Lai Y, Fang NX. Ultra-broadband illusion acoustics for space and time camouflages. *Nat Commun*. 2024;15:8046.
43. Steckel J, Boen A, Peremans H. Broadband 3-D sonar system using a sparse array for indoor navigation. *IEEE Trans Robot*. 2013;29(1):161–171.
44. Sutherland DA, Jackson RH, Kienholz C, Amundson JM, Dryer WP, Duncan D, Eidam EF, Motyka RJ, Nash JD. Direct observations of submarine melt and subsurface geometry at a tidewater glacier. *Science*. 2019;365(6451):369–374.
45. Xie B, Tang K, Cheng H, Liu Z, Chen S, Tian J. Coding acoustic metasurfaces. *Adv Mater*. 2017;29(6):1603507.
46. Cao W, Wu L, Zhang C, Ke J, Cheng Q, Cui T. A reflective acoustic meta-diffuser based on the coding meta-surface. *J Appl Phys*. 2019;126(19):Article 194503.
47. Fang X, Wang X, Li Y. Acoustic splitting and bending with compact coding metasurfaces. *Phys Rev Appl*. 2019;11(6):Article 064033.
48. Zhang Y, Xie B, Liu W, Cheng H, Chen S, Tian J. Anomalous reflection and vortex beam generation by multi-bit coding acoustic metasurfaces. *Appl Phys Lett*. 2019;114(9):Article 091905.
49. Zhang Y, Cheng H, Tian J, Chen S. Frequency-selected bifunctional coding acoustic metasurfaces. *Phys Rev Appl*. 2020;14(6):Article 064057.
50. Cao W, Zhang C, Wu L, Guo K, Ke J, Cui T, Cheng Q. Tunable acoustic metasurface for three-dimensional wave manipulations. *Phys Rev Appl*. 2021;15(2):Article 024026.
51. Cui X, Shi J, Liu X, Lai Y. A panel acoustic energy harvester based on the integration of acoustic metasurface and Helmholtz resonator. *Appl Phys Lett*. 2021;119(25): Article 253903.
52. Zhang Z, Jia Y, Jiang W, Zhang X, Qiu C-w, Cui T. Programming reflected and transmitted sound behaviors based on motor-driven digital metasurface. *Adv Funct Mater*. 2024;34(48):2411403.
53. Potton RJ. Reciprocity in optics. *Rep Prog Phys*. 2004;67(5):717–754.
54. Shi Y, Yu Z, Fan S. Limitations of nonlinear optical isolators due to dynamic reciprocity. *Nat Photonics*. 2015;9(6):388–392.
55. Sounas DL, Alù A. Non-reciprocal photonics based on time modulation. *Nat Photonics*. 2017;11(12):774–783.
56. Shi J, Liu C, Guo C, Chu H, Liu X, Christensen J, Lai Y. Broadband acoustic metaveils for configurable camouflage. *Phys Rev Appl*. 2022;18(6):Article 064064.
57. Chu H, Xiong X, Gao Y-J, Luo J, Jing H, Li C-Y, Ruwen Peng M, Wang YL. Diffuse reflection and reciprocity-protected transmission via a random-flip metasurface. *Sci Adv*. 2021;7(37):Article eabj0935.
58. Chu H, Xiong X, Fang NX, Wu F, Jia R, Peng R, Wang M, Lai Y. Matte surfaces with broadband transparency enabled by highly asymmetric diffusion of white light. *Sci Adv*. 2024;10(11):Article eadm8061.
59. Yang Z, Gao F, Shi X, Lin X, Gao Z, Chong Y, Zhang B. Topological acoustics. *Phys Rev Lett*. 2015;114(11): Article 114301.
60. Lu J, Qiu C, Ke M, Liu Z. Valley vortex states in sonic crystals. *Phys Rev Lett*. 2016;116(9):Article 093901.
61. Zhang Z, Tian Y, Cheng Y, Wei Q, Liu X, Christensen J. Topological acoustic delay line. *Phys Rev Appl*. 2018;9(3):Article 034032.
62. Qi Y, Qiu C, Xiao M, He H, Ke M, Liu Z. Acoustic realization of quadrupole topological insulators. *Phys Rev Lett*. 2020;124(20):Article 206601.
63. Zheng L-Y, Christensen J. Dirac hierarchy in acoustic topological insulators. *Phys Rev Lett*. 2021;127(15): Article 156401.
64. Guo Z, Li Z, Zeng K, Lu X, Ye J, Wang Z. Asymmetric hierarchical acoustic absorber at exceptional point: A loss-induced eigenvalues degeneracy system. *Phys Rev B*. 2024;109(10):Article 104113.